

# Excitons and emergent quantum phenomena in stacked 2D semiconductors

<https://doi.org/10.1038/s41586-021-03979-1>

Nathan P. Wilson<sup>1,2,3</sup>, Wang Yao<sup>4,5</sup>, Jie Shan<sup>6</sup> & Xiaodong Xu<sup>1,7</sup>✉

Received: 11 February 2021

Accepted: 1 September 2021

Published online: 17 November 2021

 Check for updates

The design and control of material interfaces is a foundational approach to realize technologically useful effects and engineer material properties. This is especially true for two-dimensional (2D) materials, where van der Waals stacking allows disparate materials to be freely stacked together to form highly customizable interfaces. This has underpinned a recent wave of discoveries based on excitons in stacked double layers of transition metal dichalcogenides (TMDs), the archetypal family of 2D semiconductors. In such double-layer structures, the elegant interplay of charge, spin and moiré superlattice structure with many-body effects gives rise to diverse excitonic phenomena and correlated physics. Here we review some of the recent discoveries that highlight the versatility of TMD double layers to explore quantum optics and many-body effects. We identify outstanding challenges in the field and present a roadmap for unlocking the full potential of excitonic physics in TMD double layers and beyond, such as incorporating newly discovered ferroelectric and magnetic materials to engineer symmetries and add a new level of control to these remarkable engineered materials.

The rich excitonic physics found in semiconducting nanostructures provides fertile ground to explore many-body effects<sup>1–5</sup> and engineer quantum technologies<sup>6–10</sup>. This versatility stems from the dual role of excitons, which simultaneously serve as interacting quasiparticles for studying many-body physics while facilitating strong light–matter coupling for optical excitation, control and readout. A prototypical example of this can be found in quantum wells (QWs) and coupled QWs (CQWs) based on group III–V semiconductors. Thanks in part to the high crystalline quality and precision of epitaxial growth, excitons in III–V QWs have been used to realize a wide variety of quantum effects and phases. Examples include the emergence of macroscopic order<sup>11</sup> and spontaneous coherence<sup>12</sup> of the exciton gas, observation of quantum degenerate gases<sup>1,3,13</sup>, many-body interactions in superlattices<sup>14,15</sup>, Berry phase phenomena<sup>16</sup>, and novel many-body effects of cavity-coupled polaritons<sup>17</sup>.

Many of the attributes of III–V QWs that have enabled these discoveries are also exemplified in two-dimensional (2D) direct-bandgap semiconductors such as monolayer transition metal dichalcogenides (TMDs; for example, MoS<sub>2</sub>, WSe<sub>2</sub>). They can be synthesized and isolated in monolayer form with exceptional crystal quality<sup>18</sup> and possess drastically enhanced Coulomb interactions compared to three-dimensional semiconductors, a result of reduced dielectric screening and enhanced quantum confinement in two dimensions<sup>19–24</sup>. This gives rise to tightly bound excitons at the K-point valleys in the Brillouin zone (Fig. 1a). These excitons couple strongly to light and persist to room temperature<sup>22</sup>, and are endowed with strong many-body interactions<sup>25</sup>. TMD monolayers also host unique coupled spin/valley physics<sup>26</sup>, which provides for the realization of dynamic manipulation of valley degrees of freedom with circularly and linearly polarized light<sup>27–30</sup> (Fig. 1a). Further control of excitons is afforded by their solid state environment, allowing

for electrostatic manipulation via gating<sup>25,31,32</sup> and control of Coulomb interactions by dielectric engineering<sup>33–35</sup>. For the former, gate-induced charges bind to the bosonic neutral excitons to form charged fermionic triions and Fermi polarons at low and high charge density<sup>36,37</sup>, respectively, enabling the study of excitonic phases with either bosonic or fermionic statistics. Regarding dielectric engineering, Coulomb interactions in two dimensions are subject to substantial non-local screening from their surrounding dielectric environment<sup>38</sup> that can, for example, modify exciton binding energy. Excitons in TMDs can thereby be used as a sensitive probe of their dielectric environment<sup>39–43</sup>.

The fabrication of 2D materials has long been lauded for its accessibility, requiring only adhesive tape and silicon wafers to exfoliate monolayer materials<sup>44</sup>. Without a doubt, this has played a vital role in the rapid growth of the field. Meanwhile, similarly accessible techniques for assembling multilayer structures from exfoliated 2D materials have developed to the point that they can reliably produce clean interfaces between stacked 2D layers<sup>45–47</sup>. Layers can be stacked with precise positional and rotational control. This has enabled remarkable discoveries based on customized van der Waals (vdW) interfaces, particularly in double-layer systems consisting of two stacked monolayers with identical or similar crystal lattices—termed homo- and heterobilayers, respectively (Fig. 1b). These discoveries span a broad spectrum of topics central to modern solid-state physics, including exotic variants of the Hall effect<sup>48–50</sup>, superconductivity and topological states in twisted graphene<sup>51–53</sup>, and excitons trapped in periodic moiré potentials<sup>54–57</sup>. Furthermore, the enhanced Coulomb interaction in two dimensions leads to highly tunable many-body states in TMD homo- and heterobilayers<sup>58–61</sup>. At the same time, the relatively low mass of excitons compared to atoms, along with the high binding energy of 2D

<sup>1</sup>Department of Physics, University of Washington, Seattle, WA, USA. <sup>2</sup>Walter Schottky Institute, Technical University of Munich, Garching, Germany. <sup>3</sup>Munich Centre for Quantum Science and Technology, Munich, Germany. <sup>4</sup>Department of Physics, University of Hong Kong, Hong Kong, China. <sup>5</sup>HKU-UCAS Joint Institute of Theoretical and Computational Physics at Hong Kong, Hong Kong, China. <sup>6</sup>School of Applied and Engineering Physics, Cornell University, Ithaca, NY, USA. <sup>7</sup>Department of Materials Science and Engineering, University of Washington, Seattle, WA, USA.  
✉e-mail: xuxd@uw.edu

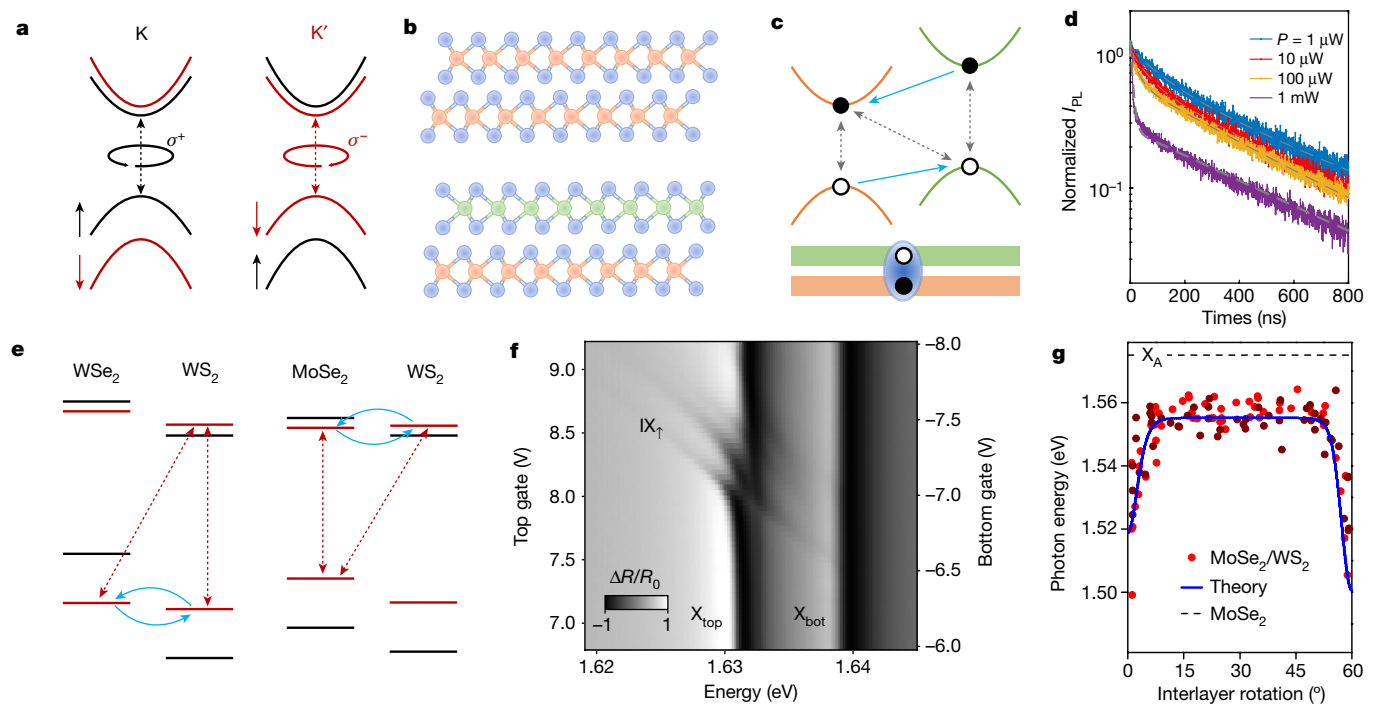


**Fig. 1 | Excitons in TMD double layers.** **a**, The spin-split conduction and valence bands in TMDs give rise to spin–valley locking and an optical selection rule for circularly polarized light, with the K (K') valley coupling to  $\sigma^+$  ( $\sigma^-$ ) polarized light. Electron spin in a given band is represented by black (spin up) or red (spin down). **b**, Examples of TMD double layers viewed from within the plane, including an AA' stacked homobilayer (top) and AB stacked heterobilayer (bottom). Orange and green dots represent different transition metal atoms, and blue dots represent chalcogens. **c**, Schematic of interband transitions in a double layer with type-II band alignment. Grey arrows indicate allowed optical transitions, and dashed blue arrows between the two layers indicate interlayer hopping. A real-space diagram of the lowest energy (interlayer) exciton is shown below. **d**, Interlayer exciton PL intensity decay following pulsed excitation across a range of excitation densities<sup>72</sup>. The fast initial decay under dense excitation is the result of many-body interactions (see the ‘Many-body interactions’ section). **e**, Resonantly enhanced interlayer

hybridization of TMD double layers can result from interlayer charge hopping (blue arrows) in both the valence (left) and conduction (right) bands for certain combinations of TMDs. Such band alignment yields nearly degenerate intra- and interlayer exciton species (red arrows). **f**, Hybridization of inter- and intralayer excitons in a TMD homobilayer observed through differential reflectance spectroscopy<sup>61</sup>. As the IX (diagonal lines) are Stark-tuned through the intralayer exciton resonances ( $X_{top}$  and  $X_{bot}$ ) by a vertical electric field, anticrossing of the inter- and intralayer species occurs. Simultaneously, the IX gains oscillator strength as it hybridizes with the intralayer excitons. The multiple IX resonances originate from superlattice effects, explored in the ‘Moiré excitons’ section. **g**, Exciton energy in an MoSe<sub>2</sub>/WS<sub>2</sub> heterobilayer varies with twist angle due to resonantly enhanced interlayer hybridization near 0° and 60° interlayer alignment<sup>57</sup>. Reproduced with permission from: **d**, ref.<sup>72</sup>, AAAS; **g**, ref.<sup>57</sup>, Springer Nature Ltd. Adapted with permission from: **f**, ref.<sup>61</sup>, Springer Nature Ltd.

excitons compared to those found in III–V semiconductors yields a high degeneracy temperature<sup>62,63</sup>. This Review will focus on such emergent excitonic phenomena in TMD double layers and discuss some of the many promising opportunities to further explore and develop this unique material system.

## Semiconducting double layers

The key distinction between naturally exfoliated bilayers of 2D materials and artificially stacked vdW double layers is the modulation of interlayer coupling due to their incommensurate stacking<sup>64</sup>. Incommensurability in double layers is either due to relative interlayer rotation and, in the case of heterobilayers, lattice mismatch. Interlayer coupling can be further controlled by insertion of an atomically thin layer of insulating hexagonal boron nitride (hBN) between the TMD layers<sup>61,65</sup>, analogous to the barrier layer in a CQW. In conventional epitaxial heterostructures, atomic diffusion and lattice mismatch at heterointerfaces result in chemical and structural defects which reduce sample quality<sup>66–68</sup>. However, vdW structures largely circumvent these problems since the layers are not chemically bonded, enabling incommensurate stacking of pristine 2D layers. Indeed, as we will explore in this article, the interplay between lattice mismatch and interlayer electronic coupling is at the heart of many intriguing phenomena in TMD double layers.

One such phenomenon is the formation of interlayer excitons (IXs)<sup>69,70</sup>, in which the wavefunction of the exciton spans both layers, analogous to the spatially indirect excitons found in CQWs. IX formation is inherent in TMD double layers due to interlayer hybridization, which delocalizes electron ( $e$ ) or hole ( $h$ ) wavefunctions across both layers. However, in heterobilayers and biased homobilayers of TMDs with type-II band alignment, K-point electrons are confined almost entirely to one layer and holes to the other by the conduction and valence band offsets, respectively (Fig. 1c)<sup>71</sup>. The resulting IXs are endowed with an out-of-plane electric dipole moment, allowing for Stark tuning over a broad spectral range<sup>65,72</sup>. Since the  $e$  and  $h$  wavefunctions are localized to opposite layers<sup>73</sup>, their overlap is vanishingly small, leading to a substantially lower oscillator strength than intralayer excitons in TMDs<sup>74</sup>. As a result, the IXs’ radiative lifetime can be hundreds of nanoseconds longer than that of the intralayer exciton species, which recombine on picosecond timescales (Fig. 1d)<sup>69,75,76</sup>. Furthermore, the  $e$ – $h$  exchange interactions, which are the primary valley depolarization mechanism for excitons, are also suppressed by interlayer separation of the  $e$ – $h$  pair, endowing IX with a microsecond-scale valley lifetime<sup>75,77,78</sup>.

Distinct from epitaxial systems in which adjacent growth layers are typically crystallographically aligned, stacked vdW layers can be freely rotated relative to one another during assembly. This is especially consequential in determining the properties of TMD double layers since

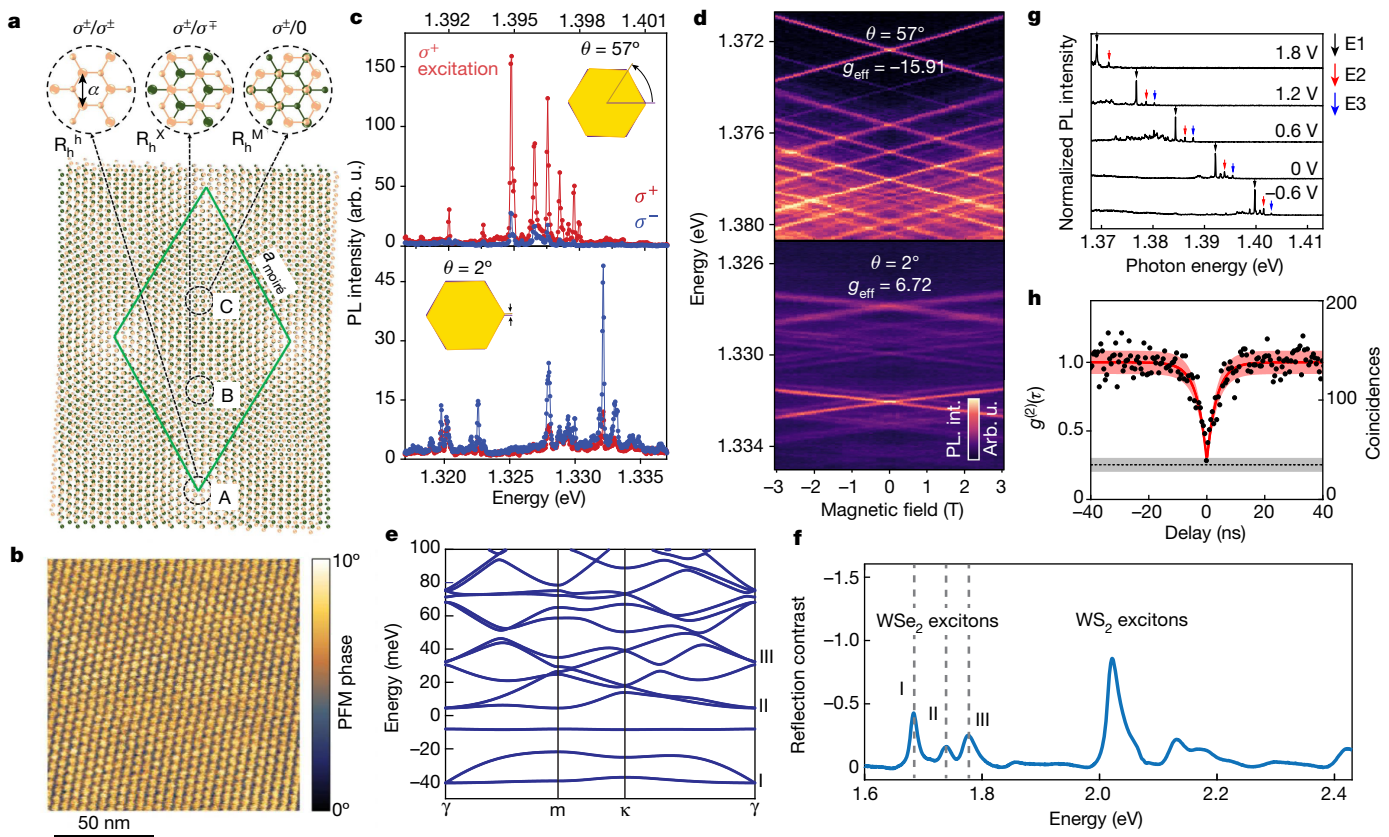


**Fig. 2 | Moiré excitons.** **a**, A moiré pattern formed by two closely aligned TMD lattices (near 0°), with the moiré unit cell outlined in green<sup>84</sup>. The three high-symmetry points of the moiré unit cell (A, B and C) are circled. They can be uniquely described by their different R-type stacking based on the alignment of the hexagonal hole (h), chalcogen atom (X), or metal atom (M) of the top layer with the hexagonal hole of the lower layer. The local stacking order determines the optical selection rule for circularly polarized light at a given point. For excitation helicity of  $\sigma^+$ , emission helicity of  $\sigma^\pm(\sigma^-)$  results from IX recombination at the A (B) site. The optical dipole at the C site points out of plane, resulting in zero emission in the out-of-plane direction. **b**, Moiré pattern of a twisted WSe<sub>2</sub>/MoSe<sub>2</sub> heterobilayer imaged by PFM phase signal<sup>91</sup>. **c**, Circularly polarized PL of moiré IX for H-type (top) and R-type (bottom) stacked WSe<sub>2</sub>/MoSe<sub>2</sub> heterobilayers. The two stacking configurations result in

opposite selection rules<sup>54</sup>. **d**, The distinct effective Landé g factors ( $g_{\text{eff}}$ ) of moiré IX in H-type (top) and R-type (bottom) stacked WSe<sub>2</sub>/MoSe<sub>2</sub> heterobilayers manifest through magnetic-field-dependent PL<sup>54</sup>. **e**, **f**, Calculated moiré exciton dispersion in a WSe<sub>2</sub>/WS<sub>2</sub> heterobilayer, with distinct optically allowed transitions denoted I–III (e), which are observed by reflectance spectroscopy in f<sup>55</sup>. **g**, Stark tuning of moiré IX in a pure electric field generated by symmetric gate electrodes, absent from charge doping effects<sup>97</sup>. **h**, Second-order photon correlation measurement of light from a single moiré IX spectral peak, showing the photon antibunching characteristic of single-photon emitters<sup>97</sup>. Adapted with permission from: **a**, ref.<sup>84</sup>, AAAS; **b**, ref.<sup>91</sup>, Springer Nature Ltd; **c**, **d**, ref.<sup>54</sup>, Springer Nature Ltd; **e**, **f**, ref.<sup>55</sup>, Springer Nature Ltd. Reproduced with permission from: **g**, **h**, ref.<sup>97</sup>, AAAS.

it directly controls the momentum-space displacement of the valleys in opposite layers<sup>70</sup>. Interlayer rotation is therefore a useful tool to substantially tune interlayer coupling<sup>64</sup> and IX dynamics<sup>79</sup>. When band edges in the two layers are aligned in both energy and momentum, interlayer hybridization is enhanced by resonant tunnelling between layers. Energetic alignment is realized intrinsically in homobilayers<sup>61</sup>, but is also possible in heterobilayers with certain combinations of TMDs in which the band offset for either the conduction or valence band is small enough to compensate by interlayer electric bias. In other combinations of TMDs, the band offsets are compensated by the valley-spin splitting with 180° interlayer alignment<sup>57,80–82</sup> (Fig. 1e). When the resonance condition is satisfied, inter- and intralayer excitons strongly hybridize through either e or h interlayer hopping. This can be seen manifestly through the anticrossing as the IXs are tuned through the intralayer resonance by the Stark effect<sup>61,80</sup> (Fig. 1f). The hybrid excitons retain the large oscillator strength of the intralayer species while still possessing the large electric dipole of the IXs. The need for momentum conservation allows the degree of hybridization to be varied by twist angle, but is sharply maximized within  $\pm 5^\circ$  of 0° or 60° interlayer alignment<sup>57</sup> (Fig. 1g). The strong twist angle dependence is a manifestation of the band-folding effect in the resulting moiré superlattice which eases

momentum conservation. Moiré superlattice effects will be explored in more depth in the following section.

## Moiré excitons

A small interlayer twist and/or lattice mismatch in TMD double layers results in the formation of a long period superlattice known as a moiré pattern (Fig. 2a)<sup>83,84</sup>. When the two layers are nearly aligned, for example in marginally twisted homobilayers, the moiré lattice constant  $a_{\text{moiré}}$  is hundreds or thousands of sublattice constants. In this case, it becomes energetically favourable for the two layers to spontaneously reconstruct by strain to form commensurately stacked domains separated by a network of dislocations<sup>85</sup>. Such lattice reconstruction becomes less significant as  $a_{\text{moiré}}$  becomes smaller. Direct observation of moiré patterns is possible by nanoscale techniques such as scanning tunnelling microscopy (STM)<sup>86–89</sup>, microwave impedance microscopy<sup>90</sup>, transmission electron microscopy<sup>85</sup>, conductive atomic force microscopy<sup>85,86</sup>, or piezoresponse force microscopy (PFM)<sup>91</sup>. STM enables atomic-resolution topographical measurement with the added ability to measure local electronic properties. PFM can readily resolve long-period moiré patterns but is only effective in materials with

nonzero piezoelectric response, that is, those with broken inversion symmetry<sup>91</sup>. However, even in centrosymmetric materials, strain from lattice reconstruction in the moiré pattern can lead to spontaneous electric polarization, giving rise to a nonzero PFM signal (Fig. 2b). This emerging technique for moiré imaging is thus sensitive to the local strain environment of the moiré pattern as well as local symmetries, providing highly complementary information to STM studies.

When the moiré unit cell is larger than the exciton radius ( $\sim 1\text{--}3\text{ nm}$ )<sup>40,92</sup>, the  $e\text{-}h$  relative motion and exciton binding are not significantly affected by the moiré pattern, whereas the centre-of-mass motion of excitons can be treated as moving in a continuum<sup>93–95</sup> that is modified perturbatively by the spatial variation of the superlattice in several ways<sup>84,96</sup>. First, at different points in the moiré unit cell, the varying impingement of atoms on either side of the vdW gap with each other modulates the interlayer spacing, giving the double layer a corrugated topography<sup>86–88</sup>. Second, the varying interlayer atomic registry and corrugation modulate the quasiparticle gaps across the moiré unit cell, creating a periodic potential that can trap excitons at high symmetry points in the moiré supercell. Finally, as the local symmetry varies across the moiré unit cell according to the local stacking registry, the optical selection rule and optical dipole of excitons are modulated (Fig. 2a).

The depth of the moiré potential depends considerably on stacking alignment (near  $0^\circ$  or R-type versus near  $60^\circ$  degree or H-type), material combination, and exciton species (intralayer versus interlayer), ranging from a few millielectronvolts to tens of millielectronvolts<sup>84</sup>. The moiré pattern can therefore localize excitons at temperatures that are readily achieved in laboratory settings, producing an array of laterally confined moiré excitons<sup>54–57</sup>. In photoluminescence (PL) measurements, a series of narrow emission lines from moiré-confined IXs have been observed under sufficiently low excitation density, which persist to 30–40 K (refs. 54,97). There are two signatures of moiré excitons in their PL that distinguish them from other localized excitons. The first is strong circular polarization of moiré IX PL, which follows from the  $C_3$  rotational symmetry of local atomic registry at moiré trapping sites<sup>84</sup>. In each moiré supercell, there are two such high symmetry locales (A and B points) with oppositely circularly polarized valley selection rules (Fig. 2a). Depending on the relative orientation of the two layers (H- or R-type stacking), the global potential minimum is at A or B respectively, allowing for the engineering of a co- or cross-circularly polarized selection rule for the moiré IXs (Fig. 2c). The second unique signature is the stacking-dependent moiré IX Landé g factor, which is determined by the valley paring of the electron and hole involved in the radiative IX recombination (Fig. 2d).

In momentum space, the effect of the moiré pattern is to fold the dispersion into the mini Brillouin zone with size  $2\pi/a_{\text{moiré}}$  (refs. 98,99), where the moiré superlattice potential opens new gaps at the crossing points, forming new excitonic minibands (Fig. 2e)<sup>55,81,84,100</sup>. Transitions to different excitonic minibands can be observed directly by absorption spectroscopy for intralayer moiré excitons<sup>55</sup> (Fig. 2f). However, the weak oscillator strength of moiré IXs makes direct detection by absorption challenging without hybridizing them with the much stronger intralayer species (Fig. 1f)<sup>61,80</sup>.

In moiré superlattices, momentum conservation can be facilitated with the two layers each supplying their reciprocal lattice vectors, that is, by umklapp processes, which play a substantial role in electronic properties of moiré structures<sup>101</sup>. In TMD double layers, electron–phonon umklapp scattering brightens excitons that are nominally momentum indirect (that is, from transitions other than  $K\text{-}K$  or  $K\text{-}K'$ )<sup>81</sup>. In the special case of rotational misalignment of  $21.8^\circ$  or  $38.2^\circ$ , where the moiré has the smallest possible supercell ( $\sqrt{7}\times\sqrt{7}$  native unit cells), umklapp processes are instrumental in brightening the  $K\text{-}K$  (or  $K\text{-}K'$ ) transitions that are momentum-indirect in the first Brillouin zone but overlap in the second Brillouin zone<sup>54,96</sup>.

Another option to control the selection rule of moiré IXs is through electrostatic gating via the IX Stark shift<sup>61,97</sup>. As with free IXs, moiré IXs couple strongly to perpendicular electric fields, with tuning of over

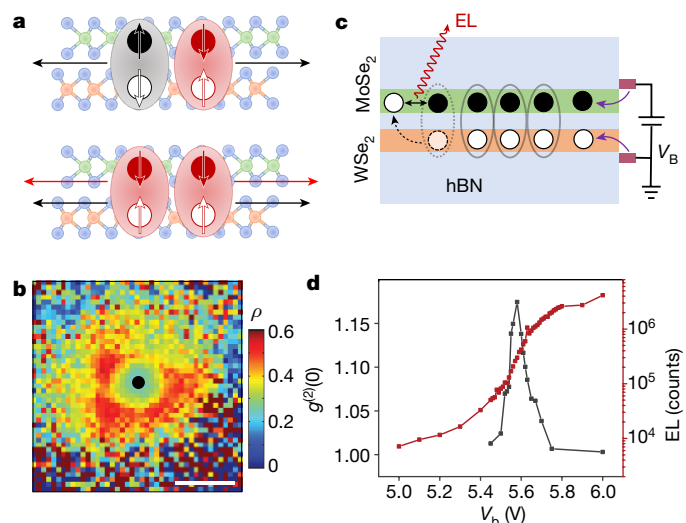


**Fig. 3 | Many-body physics of IX.** **a**, Diagram showing repulsive IX–X interactions. IXs in opposite valleys (top) experience repulsive direct Coulomb interactions (solid black arrows), while IXs in the same valley (bottom) experience additional Coulomb exchange interactions (solid red arrows). **b**, Image of PL degree of circular polarization ( $\rho$ ) of a partially valley polarized IX cloud that has diffused away from the excitation spot (black dot). Scale bar,  $2\text{ }\mu\text{m}$ . The ring-shaped valley polarization is the result of increased diffusion for IXs in the majority valley relative to the minority valley due to valley-dependent many-body interactions<sup>77</sup>. **c**, An electron–hole double layer based on a TMD heterobilayer. Electrons (solid dots) and holes (hollow dots) are injected into the individual semiconducting layer by electrodes with bias  $V_B$  (purple arrows). The electrons and holes can then bind to form an IX ensemble, whose density is controlled by  $V_B$ . A few-layer hBN barrier layer suppresses IX recombination. The electrons and holes eventually recombine following tunnelling (dashed arrow) to produce electroluminescence (EL). **d**, EL intensity and second-order temporal correlation at zero as the IX density is tuned by  $V_B$  (ref. 103), as in the device depicted in **c**. At a critical density of IXs, the EL intensity increases abruptly and acquires super-Poissonian photon statistics. Adapted with permission from: **b**, ref. <sup>77</sup>, AAAS; **d**, ref. <sup>103</sup>, Springer Nature Ltd.

40 meV having been demonstrated (Fig. 2g). Since the A and B points of the moiré lattice (Fig. 2a) have slightly different interlayer separation, the Stark shift of IXs at these points is different, allowing for the relative moiré potential at these points to be tuned by an out-of-plane electric field<sup>84</sup>. A sufficiently large electric field is predicted to switch the global potential minimum between A and B, and, since the optical selection rule is opposite at A and B, thus switch the helicity of moiré IX emission. This would be especially useful in the context of a moiré-exciton-based quantum light source. Recent experiments have demonstrated photon antibunching from moiré exciton PL, a signature for light emission by individually trapped IXs (Fig. 2h)<sup>97</sup>. Combined with the energy and helicity control afforded by the Stark effect, moiré IXs may serve as a highly tunable source for circularly polarized single photons.

## Many-body interactions

Exciton–exciton interactions in TMD monolayers and double layers have a strong, repulsive Coulomb exchange part that occurs between excitons within the same valley (Fig. 3a)<sup>102</sup>. Notably, the exchange interactions are several orders of magnitude stronger than the direct Coulomb interaction for neutral intralayer excitons. However, since IXs possess an out-of-plane electric dipole moment, the valley-independent direct Coulomb interaction corresponds to a strong dipolar repulsion between IXs, which can have comparable magnitude to the exchange part. The presence of both valley-dependent and valley-independent many-body interactions enables control of population dynamics by both the density

and valley polarization of an optically generated IX cloud. For example, in a partially valley polarized IX cloud, the majority valley component will diffuse more quickly than the minority component, resulting in a ring-shaped valley texture around the excitation spot (Fig. 3b)<sup>77</sup>. The observation of valley-dependent IX diffusion is made possible by their long population and valley lifetime, which allows for long-range diffusion. The long lifetime of IXs also allows them to cool substantially following optical injection and for a dense quasi-equilibrium population to be established under continuous illumination.

Dense and cold IX populations can also be created electrically by direct injection of electrons and holes into opposite layers of a TMD double layer (Fig. 3c)<sup>74</sup>. Carriers in the strongly interacting  $e-h$  double layer then bind to form IXs. Since IX formation in this case happens without interlayer charge transfer, the only electronic heating is from charge injection. Evidence of IX quasi-condensation was recently reported in WSe<sub>2</sub>/MoSe<sub>2</sub> heterobilayers employing this electrical injection scheme<sup>103</sup>. To suppress IX recombination, a thin insulating hBN layer was inserted between the TMD layers. The presence of the IX quasi-condensate was then inferred from critical behaviour in intralayer exciton electroluminescence (EL) that is brought about by the enhanced tunnelling of the hole of an IX to the  $e$  layer. Above a critical  $e/h$  density, the EL intensity increases rapidly and is accompanied by a switch to super-Poissonian photon statistics (Fig. 3d). These phenomena persist above 100 K, in good agreement with the predicted IX degeneracy temperature in this system. Signatures of IX degeneracy have also been reported in optically pumped TMD double layers<sup>104</sup>. At certain excitation densities and below a critical temperature, the coherence time of the IX increases abruptly while the spectral linewidth of the IX PL decreases.

Despite these advances, macroscopic coherence of IX gases, as has been previously observed in exciton gases in CQWs<sup>12</sup>, remains to be investigated as inhomogeneity introduced by imperfect moiré patterns and extrinsic environmental disorder can pose challenges. We also note that the IX gases studied in the experiments described above are necessarily out of equilibrium and inevitability decay. On the other hand, equilibrium IX condensation becomes possible when the type-II bandgap can be engineered to be smaller than the binding energy, allowing interlayer  $e-h$  pairs to be created spontaneously. Such a system can host a rich phase diagram from the competition of Coulomb interaction and quantum tunnelling in bilayer TMDs that favour orthogonal  $e-h$  pairing channels, with gate switchability from an exciton superfluid to a quantum anomalous Hall insulator<sup>105</sup>.

Lasing based on IXs in TMD heterobilayers has also been demonstrated<sup>106,107</sup>. Their type-II band structure is an effective four-level electronic system, with the two intralayer excitons (one in each layer) as the upper excited levels, and the IX as the lower excited level. Either intralayer exciton level can be efficiently pumped by resonant excitation owing to their large oscillator strength. This is followed by fast relaxation to the long-lived IX level. However, because the oscillator strength of IX is several orders of magnitude weaker than the intralayer exciton, lasing requires that the heterobilayer be efficiently coupled to an optical cavity. The transfer of 2D structures onto optical cavities, including nanostructured photonic cavities, is made relatively straightforward by vdW fabrication. This approach opens the door to optical control of dark states<sup>108</sup> and the study light-matter interactions in TMDs in the strongly coupled regime, as exemplified by the recent observation of moiré polaritons<sup>109</sup>.

## Correlated states in superlattices

Treatment of excitons in TMD double layers as either a local, quantum-confined system or a many-body interacting system is a useful paradigm in many contexts. Between these two limits is a regime in which both exciton quantum confinement and many-body effects are important. This regime can be realized in moiré patterns when  $a_{\text{moiré}}$  is small enough that hopping between discrete moiré trap sites is not

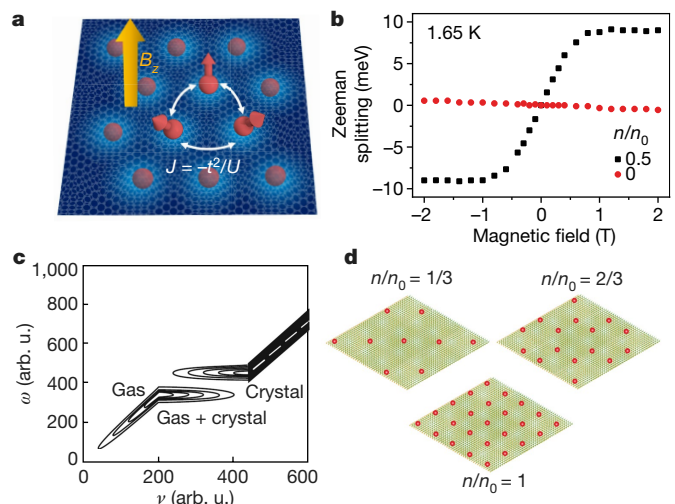


**Fig. 4 | Correlated states in superlattices.** **a, b**, Holes (red balls) in the moiré pattern of a TMD heterobilayer form a correlated insulator at half filling (**a**). The hole spins (red arrows) form a three-sublattice Hubbard model antiferromagnet with interaction strength  $J = -t^2/U$ . In a perpendicular magnetic field  $B_z$ , the spins cant towards the field vector, which can be detected via the anomalous, nonlinear Zeeman splitting of an intralayer exciton as shown in **b**<sup>58</sup>. **c**, Schematic of emission spectral distribution in energy  $\omega$  of dipolar exciton gas and crystal phases as the population density  $\nu$  increases at a fixed temperature<sup>116</sup>. Lines are isointensity contours. **d**, Possible configurations of generalized Wigner crystals. At different moiré filling factors  $n/n_0$ , they can acquire distinct lattice geometries<sup>60</sup>. Reproduced with permission from: **b**, ref.<sup>58</sup>, Springer Nature Ltd; **c**, ref.<sup>116</sup>, Springer Nature Ltd. Adapted with permission from: **d**, ref.<sup>60</sup>, Springer Nature Ltd.

negligible, but large enough that the intersite hopping integral  $t$  does not dominate on-site interaction strength  $U$  between excitons. Such a system can be described by the Hubbard model. The simplest Hubbard Hamiltonian has only two terms, corresponding to  $U$  and  $t$ , and  $U/t$  is often used as a metric for correlation strength. With the incorporation of relevant spin physics and non-local interactions, this remarkably simple model predicts a wide range of correlated phenomena such as superconductivity<sup>110</sup>, magnetism<sup>95</sup>, superfluidity and Mott insulators<sup>111</sup>, depending on lattice geometry,  $U/t$ , and spin statistics. The Hubbard model therefore offers a roadmap to engineer custom many-body Hamiltonians in artificial superlattices as an important class of quantum simulators.

A moiré pattern in TMD double layers is an example of a triangular Hubbard superlattice with positive  $U/t$  for both carriers and intra/interlayer excitons. For carriers or charged moiré trions<sup>112</sup>, the Fermi-Hubbard model is realized, while neutral moiré excitons are described by the Bose-Hubbard model. Since both carrier and exciton density can be independently controlled, correlated phases in either population can be realized in principle. For carriers, the Hubbard model predicts the experimentally observed high-temperature Mott insulating state at half filling of the first moiré miniband<sup>58–60,95</sup> and the possible formation of generalized Wigner crystals at fractional fillings<sup>60,113</sup>. Excitons interact with correlated electronic states via changes to the effective dielectric constant or enhanced exciton-carrier many-body interactions<sup>43,58–60</sup>. This enables the study of charge correlations via optical spectroscopy. Due to the presence of valley-dependent and valley-independent carrier-exciton interactions, this approach has the advantage of probing magnetic order<sup>58</sup>, spin and charge dynamics<sup>60</sup>, and other properties<sup>43</sup> that are not directly accessible by transport measurements. This approach was recently used to probe Hubbard model antiferromagnetic interactions of a Mott insulator in TMD heterobilayers via the anomalous Zeeman shift of an intralayer exciton resonance in a magnetic field (Fig. 4a, b)<sup>58</sup>.

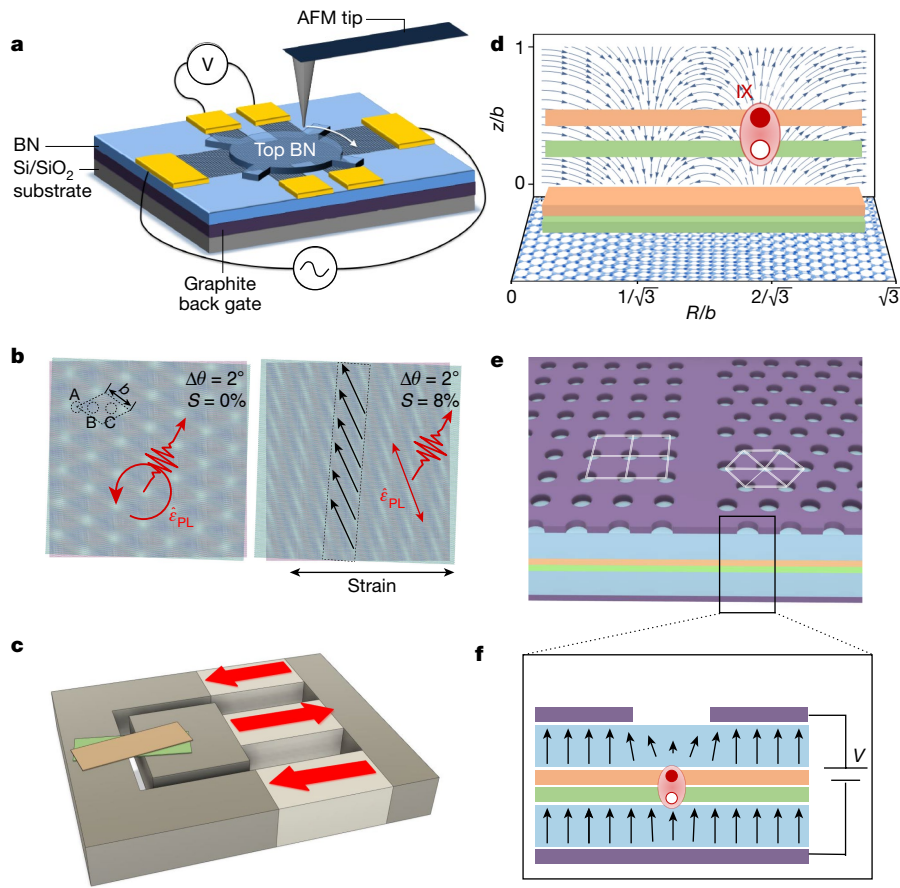


**Fig. 5 | Control of superlattice geometry.** **a**, A dynamically rotatable moiré structure consisting of a lithographically defined, rotatable hBN ‘handle’, which can be rotated relative to an underlying 2D material by an AFM tip, thereby controlling the moiré pattern they form<sup>126</sup>. **b**, A hexagonal moiré pattern in a TMD heterobilayer (left) evolves into a pseudo-stripe moiré pattern (right) due to layer differential strain, changing the optical selection rule for moiré excitons from circularly to linearly polarized (red arrows)<sup>128</sup>. **c**, Strain control of a twisted bilayer (orange and green layers). Piezoelectric actuators (white) widen a gap between two rigid plates (grey), across which the heterobilayer is suspended. A differential strain between the layers may arise if the top layer slips relative to the bottom, that is, due to the bottom layer being

anchored to the moving plates. **d**, A moiré pattern with period  $b$  in twisted hBN gives rise to a texture of electrical polarization and a stray electric field (blue arrows). IXs in a proximate bilayer (green and orange layers) can be confined by the stray electric field via the Stark effect<sup>135</sup>. **e**, **f**, A synthetic superlattice can be created by using patterned gate electrodes (purple) to create a periodically modulated electric field (black arrows). This approach allows for arbitrary superlattice geometries with a highly tunable potential to be implemented, giving convenient access to a variety of correlated phases that aren’t realizable through moiré patterns alone. Reproduced with permission from: **a**, ref.<sup>126</sup>, AAAS. Adapted with permission from: **b**, ref.<sup>128</sup>, Springer Nature Ltd; **d**, ref.<sup>135</sup>, Springer Nature Ltd.

Bosonic neutral excitons in a moiré superlattice offer another paradigm to study Hubbard model physics such as the quantum phase transition from superfluid to Mott insulators, promised by the long lifetime and strong dipolar interactions of IXs<sup>111</sup>. Despite the abundant evidence for correlated electronic states, observation of correlated excitonic states has remained elusive. This may be due in part to difficulty in achieving precise or uniform exciton filling factors. Since an optically generated exciton population varies spatially and is largely out of equilibrium, the population of equilibrated, low-energy excitons is small and can be prone to substantial number fluctuations<sup>114</sup>. Electrical injection of IXs with a tunnelling barrier between the TMD layers to reduce recombination may help overcome some of these limitations<sup>103</sup>. It may also be the case that the experimental techniques that have thus far proved useful to detect correlated electronic states are not sensitive to correlated excitonic states. Nevertheless, the rich many-body physics of moiré excitons provides ample incentive to explore new device architectures and experimental approaches to enable the detection of correlated excitonic phases.

A particularly interesting feature in the many-body phase diagram of IXs is the formation of an excitonic crystal<sup>115,116</sup>, akin to a Wigner crystal of charges. Crystallization of IXs is facilitated by their strong

repulsive dipolar interaction. In a homogeneous energy landscape, the low-density disordered gas phase and the excitonic crystal that forms at higher densities coexist over a range of densities and temperatures. This coexistence has a characteristic spectroscopic signature, with the two exciton phases having distinct transition energies (Fig. 4c). The periodic moiré potential landscape in TMD double layers may also stabilize the exciton crystal phase at lower densities than the excitonic crystal described above, as is the case for the generalized Wigner crystals of charges found in TMD double layers<sup>60,117</sup>. Generalized Wigner crystals can take on a variety of geometries, depending on filling factor (Fig. 4d). They can be probed both optically<sup>118</sup> and by a novel non-invasive STM technique, in which a nearby graphene layer acts as a proximity sensor of charge density in the Wigner crystal<sup>119</sup>. Another possibility in this direction involves IXs in trilayer heterostructures, which host dipolar IXs spread over two layers and quadrupolar IXs spread over three layers. Competing interactions between these IX species are predicted to form a rich phase diagram of ordered states<sup>120</sup>. The two independently configurable vdW interfaces in a trilayer can also be exploited to engineer quasi-periodic bichromatic superlattices<sup>121</sup>.

## Outlook

The foundational results described above establish TMD double layers as a valuable platform for studying a wide range of topics in modern physics. Building on these early successes, we highlight below the great potential for discoveries in quantum optics, correlated phases, and superlattice physics. Furthermore, we identify two main challenges going forward: the need for programmability—the ability to control moiré patterns *in situ*—and the need for more flexible and deterministic control over moiré pattern or superlattice geometry.

### A versatile quantum light source

An elementary use of the moiré excitons in TMD double layers is as a source of single photons. Absent disorder, moiré excitons form a lattice of spatially ordered quantum emitters that, in the case of the short-lived intralayer excitons, could source a bright stream of single photons. Additionally, compared to IXs, intralayer excitons have reduced long-range many-body interactions and relatively low sensitivity to disorder in the surrounding dielectric<sup>114</sup>. The former is needed to suppress unwanted correlations among quantum emitters, and the latter to realize the spectral uniformity desired for macroscopic coherent effects such as Dicke superradiance<sup>122</sup>. The emitted photons could be prepared with a predetermined circular polarization or a superposition of circular polarizations by polarized optical pumping or by electrical control<sup>84</sup>. By exploiting cascaded exciton emission, such a single-photon source could be used for the generation of polarization-entangled photon pairs<sup>84,123</sup>, a key resource for certain optical quantum technologies<sup>124</sup>. For a single-photon source, on the other hand, it is important to have addressability among the individual emitters located within an optical wavelength, which will require future technological advances in nanofabrication, for example local gating or electrical injection on the nanoscale, to achieve.

However, PL from intralayer moiré excitons has yet to be demonstrated, largely due to quenching of intralayer exciton emission by the much faster charge hopping that occurs at type-II interfaces. Engineering heterointerfaces with type-I band alignment for layer confinement of intralayer moiré excitons is therefore desirable. Twisted homobilayers may also offer a route to realize bright moiré intralayer excitons if a momentum-direct bandgap can be engineered, for which H-type MoTe<sub>2</sub> may be a possibility<sup>125</sup>. An extrinsic superlattice potential proximity-coupled to a monolayer TMD—explored in more detail below—may also prove useful in this context.

### Programmable superlattices

Another immediate opportunity is to explore *in situ* control of moiré geometry, and thus the associated properties of moiré excitons and rich charge orders. Dynamic rotational control of twisted 2D materials (Fig. 5a), such as graphene and hBN, has indicated the power of this approach to control moiré geometry<sup>126,127</sup>. So far, such dynamic rotation can only be done at room temperature with selected materials. It remains to be seen whether it can be generalized to TMDs or implemented at low temperature. Another approach is to tune moiré geometry by strain. Recent experiments have revealed that the built-in strain can be large enough to distort the moiré into a quasi-one-dimensional pattern in MoSe<sub>2</sub>/WSe<sub>2</sub> heterobilayers, which changes the moiré exciton optical selection rule from circular to linear<sup>128</sup> (Fig. 5b). *In situ* strain control of the moiré pattern, compatible with low temperature, would be powerful for dynamic control of moiré physics (Fig. 5c). Last but not least, hydrostatic pressure can be an effective knob to control the interlayer coupling<sup>129,130</sup>, and thereby the interlayer excitonic properties<sup>131</sup> associated with moiré effects.

Yet another fruitful direction is to couple moiré excitons to other order parameters, such as ferroelectric polarization and magnetism. Recently, stacking-induced ferroelectric polarization has been reported at the interface of AB (BA) stacked hBN<sup>132–134</sup>. Twisted hBN with moiré

ferroelectric polarization would be an excellent inert substrate for introducing an extrinsic superlattice potential in monolayer TMDs or coupling to the IX dipole moment in a TMD double layer (Fig. 5d)<sup>135</sup>. We note that this approach is generalizable beyond TMDs or even 2D materials, and could even prove useful in quasi-2D semiconductor systems as well. On the other hand, stacking-induced piezoelectricity is also expected intrinsically in twisted TMD double layers<sup>136,137</sup>, which host IXs as well. The observation of coupling between IXs and electric polarization in twisted MoSe<sub>2</sub> homobilayers shows the promise of this approach<sup>138</sup>.

On the other hand, coupling to magnetic order will introduce time reversal symmetry breaking into the system to engineer exotic excitonic systems, for example, endowing excitonic minibands with a nontrivial Chern number<sup>84</sup>. This could be accomplished via a magnetic proximity effect by interfacing TMD layers with a vdW magnet, for example CrI<sub>3</sub> (ref. <sup>139</sup>). In particular, moiré patterns in 2D magnets can give rise to a magnetic texture<sup>140–142</sup>, predicted to take the form of a pattern of nanoscale domains of alternating magnetization. This magnetic texture could then be coupled to an adjacent TMD monolayer or double layer, imprinting on it a spatially textured effective Zeeman field for the valley excitons.

Such effects may also be possible in 2D semiconductors with intrinsic magnetic order. One suitable candidate for this might be CrSBr (ref. <sup>143</sup>), which hosts robust excitons with a bandgap of around 1.5 eV (ref. <sup>144</sup>), and was recently isolated in its ferromagnetic monolayer form<sup>145</sup>. On the other hand, bilayer CrSBr is an A-type antiferromagnet, in which adjacent layers have antiparallel spin polarization. This magnetic order suppresses interlayer electronic hybridization, thereby coupling electronic and excitonic properties to the magnetization<sup>146</sup>. The application of a magnetic field can align the spins in adjacent layers, which then switches on interlayer hybridization. In twisted bilayer CrSBr, the field-tunable hybridization might be exploitable to dramatically tune moiré effects *in situ*. Moreover, CrSBr is a member of a family of 2D magnetic semiconductors which host diverse magnetic orders and are predicted to form type-II heterojunctions which could potentially host IXs in many combinations<sup>147</sup>.

### Beyond moiré patterns

A fundamental challenge in vdW assembly is the introduction of non-uniform strain into the layers during assembly, which leads to an inhomogeneous moiré pattern<sup>85,91,128,148,149</sup>. This introduces disorder that must be taken into account in the exploration of correlated phenomena in the superlattice. A second problem in the implementation of superlattices via moiré patterns is that the geometry of the superlattice—both periodicity and lattice shape—are constrained by the choice of materials. The ability to realize different lattice geometries is key to unlocking the diverse many-body phase diagram expected from moiré patterns<sup>150</sup>. One possible solution to both of these problems is to define a superlattice based on extrinsic potentials, akin to the use of optical lattices to trap cold atoms<sup>151</sup>. In condensed matter, this has been successfully demonstrated using patterned gate electrodes or gate dielectrics to imprint a spatially varying electric field or potential on a semiconductor layer<sup>15,152–154</sup>. This has been recently demonstrated as a method to trap IXs in TMD heterobilayers<sup>155</sup> using lithographically patterned graphene gates (Fig. 5e,f), achieving trapping potentials of up to 50 meV. Using this approach, superlattices with diverse geometry can be achieved independent of material, even adjoining multiple superlattice geometries on a single sample to form lateral interfaces between different correlated phases. However, there are substantial challenges that must be overcome, namely the resolution limitations of conventional lithography. To reliably load single excitons and guarantee homogeneous filling, the trap sites must approach the length scale of the exciton radius, only a few nanometres, which will require the use of innovative high-resolution lithography techniques.

# Review

Overall, we envision that the continued development of nanofabrication techniques and *in situ* controls for vdW double layers will play a significant role in the near-future progression of the field. While TMD double layers have proven to be a powerful system for realizing a wide range of sophisticated physical phenomena, it is clear that the exploration of new material systems and innovative device architectures will greatly expand the potential for discovery in stacked semiconductor structures. With these advances, we will be ready to explore a broad spectrum of physics, such as flat bands effects in correlation and topology, superfluidity, topological exciton bands, quantum simulations and beyond.

1. Butov, L. V., Zrenner, A., Abstreiter, G., Böhm, G. & Weimann, G. Condensation of indirect excitons in coupled AlAs/GaAs quantum wells. *Phys. Rev. Lett.* **73**, 304–307 (1994).
2. Zhu, X., Littlewood, P. B., Hybertsen, M. S. & Rice, T. M. Exciton condensate in semiconductor quantum well structures. *Phys. Rev. Lett.* **74**, 1633–1636 (1995).
3. Eisenstein, J. P. & MacDonald, A. H. Bose–Einstein condensation of excitons in bilayer electron systems. *Nature* **432**, 691–694 (2004).
4. Kleemann, N. A. J. M. et al. Many-body exciton states in self-assembled quantum dots coupled to a Fermi sea. *Nat. Phys.* **6**, 534–538 (2010).
5. Byrnes, T., Recher, P. & Yamamoto, Y. Mott transitions of exciton polaritons and indirect excitons in a periodic potential. *Phys. Rev. B* **81**, 205312 (2010).
6. Biolatti, E., Iotti, R. C., Zanardi, P. & Rossi, F. Quantum information processing with semiconductor macroatoms. *Phys. Rev. Lett.* **85**, 5647–5650 (2000).
7. Chen, P., Piermarocchi, C. & Sham, L. J. Control of exciton dynamics in nanodots for quantum operations. *Phys. Rev. Lett.* **87**, 067401 (2001).
8. De Rinaldis, S. et al. Intrinsic exciton-exciton coupling in GaN-based quantum dots: Application to solid-state quantum computing. *Phys. Rev. B* **65**, 081309(R) (2002).
9. Aharonovich, I., Englund, D. & Toth, M. Solid-state single-photon emitters. *Nat. Photon.* **10**, 631–641 (2016).
10. Ghosh, S. & Liew, T. C. H. Quantum computing with exciton-polariton condensates. *npj Quant. Inf.* **6**, 16 (2020).
11. Butov, L. V., Gossard, A. C. & Chemla, D. S. Macroscopically ordered state in an exciton system. *Nature* **418**, 751–754 (2002).
12. High, A. A. et al. Spontaneous coherence in a cold exciton gas. *Nature* **483**, 584–588 (2012).
13. Lai, C. W., Zoch, J., Gossard, A. C. & Chemla, D. S. Phase diagram of degenerate exciton systems. *Science* **303**, 503–506 (2004).
14. Remeika, M., Fogler, M. M., Butov, L. V., Hanson, M. & Gossard, A. C. Two-dimensional electrostatic lattices for indirect excitons. *Appl. Phys. Lett.* **100**, 061103 (2012).
15. Remeika, M. et al. Measurement of exciton correlations using electrostatic lattices. *Phys. Rev. B* **92**, 115311 (2015).
16. Leonard, J. R. et al. Pancharatnam-Berry phase in condensate of indirect excitons. *Nat. Commun.* **9**, 2158 (2018).
17. Smolka, S. et al. Cavity quantum electrodynamics with many-body states of a two-dimensional electron gas. *Science* **346**, 332–335 (2014).
18. Edelberg, D. et al. Approaching the intrinsic limit in transition metal diselenides via point defect control. *Nano Lett.* **19**, 4371–4379 (2019).
19. Ivanov, A. L., Haug, H. & Keldysh, L. V. Optics of excitonic molecules in semiconductors and semiconductor microstructures. *Phys. Rep.* **296**, 237–336 (1998).
20. Van Tuan, D., Yang, M. & Dery, H. Coulomb interaction in monolayer transition-metal dichalcogenides. *Phys. Rev. B* **98**, 125308 (2018).
21. Mak, K. F., Lee, C., Hone, J., Shan, J. & Heinz, T. F. Atomically thin MoS<sub>2</sub>: a new direct-gap semiconductor. *Phys. Rev. Lett.* **105**, 136805 (2010).
22. He, K. et al. Tightly bound excitons in monolayer WSe<sub>2</sub>. *Phys. Rev. Lett.* **113**, 026803 (2014).
23. Wang, G. et al. Giant enhancement of the optical second-harmonic emission of WSe<sub>2</sub> monolayers by laser excitation at exciton resonances. *Phys. Rev. Lett.* **114**, 097403 (2015).
24. Stier, A. V., McCreary, K. M., Jonker, B. T., Kono, J. & Crooker, S. A. Exciton diamagnetic shifts and valley Zeeman effects in monolayer WS<sub>2</sub> and MoS<sub>2</sub> to 65 tesla. *Nat. Commun.* **7**, 10643 (2016).
25. Berkelsbach, T. C., Hybertsen, M. S. & Reichman, D. R. Theory of neutral and charged excitons in monolayer transition metal dichalcogenides. *Phys. Rev. B* **88**, 045318 (2013).
26. Xiao, D., Liu, G.-B., Feng, W., Xu, X. & Yao, W. Coupled spin and valley physics in monolayers of MoS<sub>2</sub> and other group-VI dichalcogenides. *Phys. Rev. Lett.* **108**, 196802 (2012).
27. Xiao, D. et al. Coupled spin and valley physics in monolayers of MoS<sub>2</sub> and other group-VI dichalcogenides. *Phys. Rev. Lett.* **108**, 196802 (2012).
28. Mak, K. F., He, K., Shan, J. & Heinz, T. F. Control of valley polarization in monolayer MoS<sub>2</sub> by optical helicity. *Nat. Nanotechnol.* **7**, 494–498 (2012).
29. Jones, A. M. et al. Optical generation of excitonic valley coherence in monolayer WSe<sub>2</sub>. *Nat. Nanotechnol.* **8**, 634–638 (2013).
30. Xu, X., Yao, W., Xiao, D. & Heinz, T. F. Spin and pseudospins in layered transition metal dichalcogenides. *Nat. Phys.* **10**, 343–350 (2014).
31. Mak, K. F. et al. Tightly bound trions in monolayer MoS<sub>2</sub>. *Nat. Mater.* **12**, 207–211 (2013).
32. Ross, J. S. et al. Electrically tunable excitonic light-emitting diodes based on monolayer WSe<sub>2</sub> p-n junctions. *Nat. Nanotechnol.* **9**, 268–272 (2014).
33. Raja, A. et al. Coulomb engineering of the bandgap and excitons in two-dimensional materials. *Nat. Commun.* **8**, 15251 (2017).
34. Chaves, A. et al. Bandgap engineering of two-dimensional semiconductor materials. *npj 2D Mater. Appl.* **4**, 29 (2020).
35. Peimyoo, N. et al. Engineering dielectric screening for potential-well arrays of excitons in 2D materials. *ACS Appl. Mater. Interfaces* **12**, 55134–55140 (2020).
36. Sidler, M. et al. Fermi polaron-polaritons in charge-tunable atomically thin semiconductors. *Nat. Phys.* **13**, 255–261 (2017).
37. Efimkin, D. K. & MacDonald, A. H. Many-body theory of trion absorption features in two-dimensional semiconductors. *Phys. Rev. B* **95**, 035417 (2017).
38. Keldysh, L. V. Coulomb interaction in thin semiconductor and semimetal films. *J. Exp. Theor. Phys.* **29**, 658–661 (1979).
39. Chernikov, A. et al. Exciton binding energy and nonhydrogenic Rydberg series in monolayer WS<sub>2</sub>. *Phys. Rev. Lett.* **113**, 076802 (2014).
40. Stier, A. V., Wilson, N. P., Clark, G., Xu, X. & Crooker, S. A. Probing the influence of dielectric environment on excitons in monolayer WSe<sub>2</sub>: insight from high magnetic fields. *Nano Lett.* **16**, 7054–7060 (2016).
41. Stier, A. V. et al. Magnetooptics of exciton Rydberg states in a monolayer semiconductor. *Phys. Rev. Lett.* **120**, 057405 (2018).
42. Raja, A. et al. Dielectric disorder in two-dimensional materials. *Nat. Nanotechnol.* **14**, 832–837 (2019).
43. Xu, Y. et al. Correlated insulating states at fractional fillings of moiré superlattices. *Nature* **587**, 214–218 (2020).
44. Novoselov, K. S. et al. Electric field in atomically thin carbon films. *Science* **306**, 666–669 (2004).
45. Kim, K. et al. Van der Waals Heterostructures with High Accuracy Rotational Alignment. *Nano Lett.* **16**, 1989–1995 (2016).
46. Frisenda, R. et al. Recent progress in the assembly of nanodevices and van der Waals heterostructures by deterministic placement of 2D materials. *Chem. Soc. Rev.* **47**, 53–68 (2018).
47. Kinoshita, K. et al. Dry release transfer of graphene and few-layer h-BN by utilizing thermoplasticity of polypropylene carbonate. *npj 2D Mater. Appl.* **3**, 22 (2019).
48. Moon, P. & Koshino, M. Energy spectrum and quantum Hall effect in twisted bilayer graphene. *Phys. Rev. B* **85**, 195458 (2012).
49. Dean, C. R. et al. Hofstadter's butterfly and the fractal quantum Hall effect in moiré superlattices. *Nature* **497**, 598–602 (2013).
50. Sharpe, A. L. et al. Emergent ferromagnetism near three-quarters filling in twisted bilayer graphene. *Science* **365**, 605–608 (2019).
51. Cao, Y. et al. Unconventional superconductivity in magic-angle graphene superlattices. *Nature* **556**, 43–50 (2018).
52. Serlin, M. et al. Intrinsic quantized anomalous Hall effect in a moiré heterostructure. *Science* **367**, 900–903 (2020).
53. Chen, G. et al. Tunable correlated Chern insulator and ferromagnetism in a moiré superlattice. *Nature* **579**, 56–61 (2020).
54. Seyler, K. L. et al. Signatures of moiré-trapped valley excitons in MoSe<sub>2</sub>/WSe<sub>2</sub> heterobilayers. *Nature* **567**, 66–70 (2019). **Demonstration of quantum-dot-like PL from moiré IXs.**
55. Jin, C. et al. Observation of moiré excitons in WSe<sub>2</sub>/WS<sub>2</sub> heterostructure superlattices. *Nature* **567**, 76–80 (2019). **Demonstration of intralayer moiré excitons and moiré minibands through reflectance spectroscopy.**
56. Tran, K. et al. Evidence for moiré excitons in van der Waals heterostructures. *Nature* **567**, 71–75 (2019).
57. Alexeev, E. M. et al. Resonantly hybridized excitons in moiré superlattices in van der Waals heterostructures. *Nature* **567**, 81–86 (2019). **Demonstration and analysis of resonant interlayer hybridization in twisted TMD heterobilayers.**
58. Tang, Y. et al. Simulation of Hubbard model physics in WSe<sub>2</sub>/WS<sub>2</sub> moiré superlattices. *Nature* **579**, 353–358 (2020). **Realization of Hubbard-model correlated antiferromagnetism in the moiré pattern of a TMD double layer.**
59. Wang, L. et al. Correlated electronic phases in twisted bilayer transition metal dichalcogenides. *Nat. Mater.* **19**, 861–866 (2020).
60. Regan, E. C. et al. Mott and generalized Wigner crystal states in WSe<sub>2</sub>/WS<sub>2</sub> moiré superlattices. *Nature* **579**, 359–363 (2020). **Realization of generalized Wigner crystals in TMD heterobilayers.**
61. Shimazaki, Y. et al. Strongly correlated electrons and hybrid excitons in a moiré heterostructure. *Nature* **580**, 472–477 (2020). **Demonstration of hybrid inter/intralayer excitons and moiré excitons in a TMD homobilayer.**
62. Wu, F. C., Xue, F. & Macdonald, A. H. Theory of two-dimensional spatially indirect equilibrium exciton condensates. *Phys. Rev. B* **92**, 165121 (2015).
63. Fogler, M. M., Butov, L. V. & Novoselov, K. S. High-temperature superfluidity with indirect excitons in van der Waals heterostructures. *Nat. Commun.* **5**, 4555 (2014).
64. Liu, K. et al. Evolution of interlayer coupling in twisted molybdenum disulfide bilayers. *Nat. Commun.* **5**, 4966 (2014).
65. Calman, E. V. et al. Indirect excitons in van der Waals heterostructures at room temperature. *Nat. Commun.* **9**, 1895 (2018).
66. Matthews, J. W. & Blakeslee, A. E. Defects in epitaxial multilayers: I. Misfit dislocations. *J. Cryst. Growth* **27**, 118–125 (1974).
67. Matthews, J. W. & Blakeslee, A. E. Defects in epitaxial multilayers. II. Dislocation pile-ups, threading dislocations, slip lines and cracks. *J. Cryst. Growth* **29**, 273–280 (1975).
68. Matthews, J. W. & Blakeslee, A. E. Defects in epitaxial multilayers. III. Preparation of almost perfect multilayers. *J. Cryst. Growth* **32**, 265–273 (1976).
69. Rivera, P. et al. Observation of long-lived interlayer excitons in monolayer MoSe<sub>2</sub>–WSe<sub>2</sub> heterostructures. *Nat. Commun.* **6**, 6242 (2015). **Demonstration of IX PL and dynamics in a TMD heterobilayer.**
70. Heo, H. et al. Interlayer orientation-dependent light absorption and emission in monolayer semiconductor stacks. *Nat. Commun.* **6**, 7372 (2015).
71. Latini, S., Winther, K. T., Olsen, T. & Thygesen, K. S. Interlayer excitons and band alignment in MoS<sub>2</sub>/hBN/WSe<sub>2</sub> van der Waals heterostructures. *Nano Lett.* **17**, 938–945 (2016).

72. Jauregui, L. A. et al. Electrical control of interlayer exciton dynamics in atomically thin heterostructures. *Science* **366**, 870–875 (2019).
- Demonstration of Stark effect and doping control of IX species, their spectra and their dynamics.**
73. Liu, G. B., Xiao, D., Yao, Y., Xu, X. & Yao, W. Electronic structures and theoretical modelling of two-dimensional group-VIB transition metal dichalcogenides. *Chem. Soc. Rev.* **44**, 2643–2663 (2015).
74. Ross, J. S. et al. Interlayer exciton optoelectronics in a 2D heterostructure p-n junction. *Nano Lett.* **17**, 638–643 (2017).
75. Kim, J. et al. Observation of ultralong valley lifetime in  $\text{WSe}_2/\text{MoS}_2$  heterostructures. *Sci. Adv.* **3**, e1700518 (2017).
76. Miller, B. et al. Long-lived direct and indirect interlayer excitons in van der Waals heterostructures. *Nano Lett.* **17**, 5229–5237 (2017).
77. Rivera, P. et al. Valley-polarized exciton dynamics in a 2D semiconductor heterostructure. *Science* **351**, 688–691 (2016).
- Study of many-body interactions of valley-polarized IX populations.**
78. Jin, C. et al. Imaging of pure spin-valley diffusion current in  $\text{WS}_2\text{-WSe}_2$  heterostructures. *Science* **360**, 893–896 (2018).
79. Zhu, H. et al. Interfacial charge transfer circumventing momentum mismatch at two-dimensional van der Waals heterojunctions. *Nano Lett.* **17**, 3591–3598 (2017).
80. Tang, Y. et al. Tuning layer-hybridized moiré excitons by the quantum-confined Stark effect. *Nat. Nanotechnol.* **2**, 52–57 (2020).
81. Ruiz-Tijerina, D. A. & Fal'ko, V. I. Interlayer hybridization and moiré superlattice minibands for electrons and excitons in heterobilayers of transition-metal dichalcogenides. *Phys. Rev. B* **99**, 125424 (2019).
82. Zhang, L. et al. Twist-angle dependence of moiré excitons in  $\text{WS}_2/\text{MoSe}_2$  heterobilayers. *Nat. Commun.* **11**, 5888 (2020).
83. Luican, A. et al. Single-layer behavior and its breakdown in twisted graphene layers. *Phys. Rev. Lett.* **106**, 126802 (2011).
84. Yu, H. et al. Moiré excitons: from programmable quantum emitter arrays to spin-orbit-coupled artificial lattices. *Sci. Adv.* **3**, e1701696 (2017).
- Calculation of the properties of moiré excitons in TMD heterobilayers, and derivation of quantum-optical properties of moiré excitons.**
85. Rosenberger, M. R. et al. Twist angle-dependent atomic reconstruction and moiré patterns in transition metal dichalcogenide heterostructures. *ACS Nano* **14**, 4550–4558 (2020).
86. Zhang, C. et al. Interlayer couplings, moiré patterns, and 2D electronic superlattices in  $\text{MoS}_2/\text{WSe}_2$  hetero-bilayers. *Sci. Adv.* **3**, e1601459 (2017).
87. Woods, C. R. et al. Commensurate-incommensurate transition in graphene on hexagonal boron nitride. *Nat. Phys.* **10**, 451–456 (2014).
88. Flores, M., Cisternas, E., Correa, J. D. & Vargas, P. Moiré patterns on STM images of graphite induced by rotations of surface and subsurface layers. *Chem. Phys.* **423**, 49–54 (2013).
89. Zhang, Z. et al. Flat bands in twisted bilayer transition metal dichalcogenides. *Nat. Phys.* **16**, 1093–1096 (2020).
90. Lee, K. et al. Ultrahigh-resolution scanning microwave impedance microscopy of moiré lattices and superstructures. *Sci. Adv.* **6**, eabd1919 (2020).
91. McGilly, L. J. et al. Visualization of moiré superlattices. *Nat. Nanotechnol.* **15**, 580–584 (2020).
92. Van Der Donck, M. & Peeters, F. M. Interlayer excitons in transition metal dichalcogenide heterostructures. *Phys. Rev. B* **98**, 115104 (2018).
93. Jung, J., Raoux, A., Qiao, Z. & Macdonald, A. H. Ab initio theory of moiré superlattice bands in layered two-dimensional materials. *Phys. Rev. B* **89**, 205414 (2014).
94. Guinea, F. & Walet, N. R. Continuum models for twisted bilayer graphene: effect of lattice deformation and hopping parameters. *Phys. Rev. B* **99**, 205134 (2019).
95. Wu, F., Lovorn, T., Tutuc, E. & MacDonald, A. H. Hubbard model physics in transition metal dichalcogenide moiré bands. *Phys. Rev. Lett.* **121**, 026402 (2018).
96. Yu, H., Wang, Y., Tong, Q., Xu, X. & Yao, W. Anomalous light cones and valley optical selection rules of interlayer excitons in twisted heterobilayers. *Phys. Rev. Lett.* **115**, 187002 (2015).
97. Baek, H. et al. Highly energy-tunable quantum light from moiré-trapped excitons. *Sci. Adv.* **6**, 8526–8537 (2020).
- Demonstration of single photon emission from moiré excitons and electric-field tunability of moiré excitons.**
98. Mucha-Kruczyński, M., Wallbank, J. R. & Fal'ko, V. I. Moiré miniband features in the angle-resolved photoemission spectra of graphene/hBN heterostructures. *Phys. Rev. B* **93**, 085409 (2016).
99. Xie, S. et al. Direct observation of distinct minibands in moiré superlattices. Preprint at <https://arxiv.org/abs/2010.07806> (2020).
100. Brem, S. et al. Hybridized intervalley moiré excitons and flat bands in twisted  $\text{WSe}_2$  bilayers. *Nanoscale* **12**, 11088–11094 (2020).
101. Wallbank, J. R. et al. Excess resistivity in graphene superlattices caused by umklapp electron-electron scattering. *Nat. Phys.* **15**, 32–36 (2019).
102. Shahnazaryan, V., Iorsh, I., Shelykh, I. A. & Kyriienko, O. Exciton-exciton interaction in transition-metal dichalcogenide monolayers. *Phys. Rev. B* **96**, 115409 (2017).
103. Wang, Z. et al. Evidence of high-temperature exciton condensation in two-dimensional atomic double layers. *Nature* **574**, 76–80 (2019).
- Study of a degenerate gas of electrically pumped IX through electroluminescence.**
104. Sigl, L. et al. Signatures of a degenerate many-body state of interlayer excitons in a van der Waals heterostack. *Phys. Rev. Res.* **2**, 042044 (2020).
105. Zhu, Q., Tu, M. W. Y., Tong, Q. & Yao, W. Gate tuning from exciton superfluid to quantum anomalous Hall in van der Waals heterobilayer. *Sci. Adv.* **5**, eaau6120 (2019).
106. Paik, E. Y. et al. Interlayer exciton laser of extended spatial coherence in atomically thin heterostructures. *Nature* **576**, 80–84 (2019).
107. Liu, Y. et al. Room temperature nanocavity laser with interlayer excitons in 2D heterostructures. *Sci. Adv.* **5**, eaav4506 (2019).
108. Latini, S., Ronca, E., De Giovannini, U., Hübener, H. & Rubio, A. Cavity control of excitons in two-dimensional materials. *Nano Lett.* **19**, 3473–3479 (2019).
109. Zhang, L. et al. Van der Waals heterostructure polaritons with moiré-induced nonlinearity. *Nature* **591**, 61–65 (2021).
110. Dagotto, E. & Riera, J. Superconductivity in the two-dimensional t-J model. *Phys. Rev. B* **46**, 12084(R) (1992).
111. Greiner, M., Mandel, O., Esslinger, T., Hänsch, T. W. & Bloch, I. Quantum phase transition from a superfluid to a Mott insulator in a gas of ultracold atoms. *Nature* **415**, 39–44 (2002).
112. Liu, E. et al. Signatures of moiré trions in  $\text{WSe}_2/\text{MoSe}_2$  heterobilayers. *Nature* **594**, 46–50 (2021).
113. Huang, X. et al. Correlated insulating states at fractional fillings of the  $\text{WS}_2/\text{WSe}_2$  moiré lattice. *Nat. Phys.* **17**, 715–719 (2021).
114. Nagler, P. et al. Interlayer exciton dynamics in a dichalcogenide monolayer heterostructure. *2D Mater.* **4**, O25112 (2017).
115. Böning, J., Filinov, A. & Bonitz, M. Crystallization of an exciton superfluid. *Phys. Rev. B* **84**, 75130 (2011).
116. Suris, R. A. Gas-crystal phase transition in a 2D dipolar exciton system. *J. Exp. Theor. Phys.* **122**, 602–607 (2016).
117. Padhi, B., Chitra, R. & Phillips, P. W. Generalized Wigner crystallization in moiré materials. *Phys. Rev. B* **103**, 125146 (2021).
118. Jin, C. et al. Stripe phases in  $\text{WSe}_2/\text{WS}_2$  moiré superlattices. *Nat. Mater.* **20**, 940–944 (2021).
119. Wang, F. et al. Imaging generalized Wigner crystal states in a  $\text{WSe}_2/\text{WS}_2$  moiré superlattice. Preprint at <https://doi.org/10.21203/rs.3.rs-390032/v1> (2021).
120. Slobodkin, Y. et al. Quantum phase transitions of trilayer excitons in atomically thin heterostructures. *Phys. Rev. Lett.* **125**, 255301 (2020).
121. Tong, Q., Chen, M., Xiao, F., Yu, H. & Yao, W. Interferences of electrostatic moiré potentials and bichromatic superlattices of electrons and excitons in transition metal dichalcogenides. *2D Mater.* **8**, O25007 (2021).
122. Dicke, R. H. Coherence in spontaneous radiation processes. *Phys. Rev.* **93**, 99–110 (1954).
123. Yu, H. & Yao, W. Luminescence anomaly of dipolar valley excitons in homobilayer semiconductor moiré superlattices. *Phys. Rev. X* **11**, 021042 (2021).
124. Rezai, M., Wrachtrup, J. & Gerhardt, I. Polarization-entangled photon pairs from a single molecule. *Optica* **6**, 34–40 (2019).
125. Lezama, I. G. et al. Indirect-to-direct band gap crossover in few-layer  $\text{MoTe}_2$ . *Nano Lett.* **15**, 2336–2342 (2015).
126. Ribeiro-Palau, R. et al. Twistable electronics with dynamically rotatable heterostructures. *Science* **361**, 690–693 (2018).
- Realization of in situ control of twist angle in a vdW heterostructure.**
127. Yao, K. et al. Enhanced tunable second harmonic generation from twistable interfaces and vertical superlattices in boron nitride homostructures. *Sci. Adv.* **7**, eabe8691 (2021).
128. Bai, Y. et al. Excitons in strain-induced one-dimensional moiré potentials at transition metal dichalcogenide heterojunctions. *Nat. Mater.* **19**, 1068–1073 (2020).
129. Song, T. et al. Switching 2D magnetic states via pressure tuning of layer stacking. *Nat. Mater.* **18**, 1298–1302 (2019).
130. Yankowitz, M. et al. Tuning superconductivity in twisted bilayer graphene. *Science* **363**, 1059–1064 (2019).
131. Xia, J. et al. Strong coupling and pressure engineering in  $\text{WSe}_2\text{-MoSe}_2$  heterobilayers. *Nat. Phys.* **17**, 92–98 (2020).
132. Woods, C. R. et al. Charge-polarized interfacial superlattices in marginally twisted hexagonal boron nitride. *Nat. Commun.* **12**, 347 (2021).
133. Stern, M. V. et al. Interfacial ferroelectricity by van der Waals sliding. *Science* **372**, 1462–1466 (2021).
134. Yasuda, K., Wang, X., Watanabe, K., Taniguchi, T. & Jarillo-Herrero, P. Stacking-engineered ferroelectricity in bilayer boron nitride. *Science* **372**, 1458–1462 (2021).
135. Zhao, P., Xiao, C. & Yao, W. Universal superlattice potential for 2D materials from twisted interface inside h-BN substrate. *npj 2D Mater. Appl.* **5**, 38 (2021).
136. Weston, A. et al. Atomic reconstruction in twisted bilayers of transition metal dichalcogenides. *Nat. Nanotechnol.* **15**, 592–597 (2020).
137. Enaldev, V. V., Ferreira, F., Magorrian, S. J. & Fal'ko, V. I. Piezoelectric networks and ferroelectric moiré superlattice domains in twistronic  $\text{WS}_2/\text{MoS}_2$  and  $\text{WSe}_2/\text{MoSe}_2$  bilayers. *2D Mater.* **8**, O25030 (2020).
138. Sung, J. et al. Broken mirror symmetry in excitonic response of reconstructed domains in twisted  $\text{MoSe}_2/\text{MoSe}_2$  bilayers. *Nat. Nanotechnol.* **15**, 750–754 (2020).
139. Zhong, D. et al. Van der Waals engineering of ferromagnetic semiconductor heterostructures for spin and valleytronics. *Sci. Adv.* **3**, e1603113 (2017).
140. Sivadas, N., Okamoto, S., Xu, X., Fennie, C. J. & Xiao, D. Stacking-dependent magnetism in bilayer  $\text{CrI}_3$ . *Nano Lett.* **18**, 7658–7664 (2018).
141. Tong, Q., Liu, F., Xiao, J. & Yao, W. Skyrmiions in the Moiré of van der Waals 2D Magnets. *Nano Lett.* **18**, 7194–7199 (2018).
142. Xu, Y. et al. Emergence of a noncollinear magnetic state in twisted bilayer  $\text{CrI}_3$ . Preprint at <https://arxiv.org/abs/2103.09850> (2021).
143. Göser, O., Paul, W. & Kahle, H. G. Magnetic properties of  $\text{CrSBr}$ . *J. Magn. Magn. Mater.* **92**, 129–136 (1990).
144. Telford, E. J. et al. Layered antiferromagnetism induces large negative magnetoresistance in the van der Waals semiconductor  $\text{CrSBr}$ . *Adv. Mater.* **32**, 2003240 (2020).
145. Lee, K. et al. Magnetic order and symmetry in the 2d semiconductor  $\text{CrSBr}$ . *Nano Lett.* **21**, 3511–3517 (2021).
146. Wilson, N. P. et al. Interlayer electronic coupling on demand in a 2D magnetic semiconductor. *Nat. Mater.* <https://doi.org/10.1038/s41563-021-01070-8> (2021).
147. Wang, C. et al. A family of high-temperature ferromagnetic monolayers with locked spin-dichroism-mobility anisotropy:  $\text{MnNX}$  and  $\text{CrCX}$  ( $X = \text{Cl}, \text{Br}, \text{I}; \text{C} = \text{S}, \text{Se}, \text{Te}$ ). *Sci. Bull.* **64**, 293–300 (2019).
148. Andersen, T. I. et al. Excitons in a reconstructed moiré potential in twisted  $\text{WSe}_2/\text{WSe}_2$  homobilayers. *Nat. Mater.* **20**, 480–487 (2021).

149. Yoo, H. et al. Atomic and electronic reconstruction at the van der Waals interface in twisted bilayer graphene. *Nat. Mater.* **18**, 448–453 (2019).
150. Kennes, D. M. et al. Moiré heterostructures as a condensed-matter quantum simulator. *Nat. Phys.* **17**, 155–163 (2021).
151. Bloch, I. Ultracold quantum gases in optical lattices. *Nat. Phys.* **1**, 23–30 (2005).
152. Ismail, K., Chu, W., Yen, A., Antoniadis, D. A. & Smith, H. I. Negative transconductance and negative differential resistance in a grid-gate modulation-doped field-effect transistor. *Appl. Phys. Lett.* **54**, 460–462 (1989).
153. Forsythe, C. et al. Band structure engineering of 2D materials using patterned dielectric superlattices. *Nat. Nanotechnol.* **13**, 566–571 (2018).
154. Xu, Y. et al. Creation of moiré bands in a monolayer semiconductor by spatially periodic dielectric screening. *Nat. Mater.* **20**, 645–649 (2021).
155. Shanks, D. N. et al. Nanoscale trapping of interlayer excitons in a 2D semiconductor heterostructure. *Nano Lett.* **21**, 5641–5647 (2021).

**Acknowledgements** N.P.W. would like to thank J. J. Finley for helpful discussions. X.X. and N.P.W. acknowledge support by the US Department of Energy, Office of Science, Basic Energy Sciences, under award number DE-SC0018171. N.P.W. also acknowledges support from the Deutsche Forschungsgemeinschaft (DFG, German Research Foundation) under Germany's

Excellence Strategy—EXC-2111—390814868. W.Y. acknowledges support by the Croucher Foundation (Croucher Senior Research Fellowship), and the Research Grants Council of Hong Kong (AoE/P-701/20). J.S. acknowledges support by the US Department of Energy (DOE), Office of Science, Basic Energy Sciences (BES), under award number DE-SC0019481.

**Author contributions** X.X. and N.P.W. conceived this work. All authors contributed to the writing and preparation of the manuscript, supervised by X.X.

**Competing interests** The authors declare no competing interests.

#### Additional information

**Correspondence and requests for materials** should be addressed to Xiaodong Xu.

**Peer review information** *Nature* thanks Kristiaan De Greve, Tomasz Smolenski and the other, anonymous, reviewer(s) for their contribution to the peer review of this work.

**Reprints and permissions information** is available at <http://www.nature.com/reprints>.

**Publisher's note** Springer Nature remains neutral with regard to jurisdictional claims in published maps and institutional affiliations.

© Springer Nature Limited 2021